Chinese Chemical Letters 36 (2025) 109796

Contents lists available at ScienceDirect

Chinese Chemical Letters

journal homepage: www.elsevier.com/locate/cclet

Hexapod cobalt phosphosulfide nanorods encapsulating into multiple hetero-atom doped carbon frameworks for advanced sodium/potassium ion battery anodes

Shimei Wu[a], Yining Li[a], Lantao Chen[a], Yufei Zhang[a,*], Lingxing Zeng[b,*], Haosen Fan[a,*]

[a] School of Chemistry and Chemical Engineering, Guangzhou University, Guangzhou 510006, China
[b] College of Environmental Science and Engineering, Fujian Normal University, Fuzhou 350007, China

ARTICLE INFO

Article history:
Received 30 January 2024
Revised 23 February 2024
Accepted 19 March 2024
Available online 22 March 2024

Keywords:
Hexapod
PZS coating
Cobalt phosphosulfide
Synergistic effect
Sodium-ion batteries

ABSTRACT

Metal phosphosulfides have been recognized as advanced anode materials for sodium/potassium ion batteries due to their high theoretical capacities and the incorporation of the advantage of metal sulfides and phosphates. However, they also suffer from the shortcomings of frustrating cycling stability due to the large volume expansion and unsatisfactory electrical conductivity. Herein, hexapod cobalt phosphosulfide nanodots based nanorods encapsulating into N, P, and S hetero-atoms tri-doped carbon framework (CoP/CoS_2@NPSC) have been triumphantly designed and synthesized. The six nanorods constructed hexapod framework and multi-atom doped carbon matrix not only provides more active sites, but also contribute to maintain the structure integrity from avoiding the agglomeration of internal CoP and CoS_2 nanodots. The synergistic effect between CoP and CoS_2 components, as well as the CoP/CoS_2 and the NPSC carbon framework can improve the electrochemical conductivity. Besides, the kinetics analysis demonstrated that N/P/S tri-doping could greatly increase the interlayer distance and introduce enough active sites, which effectively facilitate the transport, adsorption, insertion and diffusion of Na^+ and K^+. CoP/CoS_2@NPSC demonstrated excellent electrochemical properties and battery performances including excellent cycle stability with 404.63 mAh/g at 5.0 A/g around 700 cycles for SIBs and 115.33 mAh/g at 5.0 A/g around 800 cycles for PIBs. This presented strategy establishes a novel and adaptable method for the integration of doped carbon with metal phosphosulfide and guides a new research approach and direction for secondary batteries electrode materials.

In recent years, the increasing numbers of portable electronics and large energy devices have led to the rapid increase in the consumption of non-renewable energy sources. Lithium-ion batteries (LIBs) have been universally exploited as the electrochemical energy pioneer on account of their excellent battery performance and significant cycling capability. However, the relative lack and uneven distribution of Li resources have restricted the enlargement of LIBs [1–4]. As emerging energy storage devices, Na^+ batteries (SIBs) and K^+ batteries (PIBs) are considered as the potential alternatives for LIBs by reason of the abundant reserves and the low costs of sodium/potassium, as well as the similar electrochemical reaction with LIBs. However, the ionic radii of both Na and K ions are larger than those of Li ions, leading to the slow diffusion dynamics issue and heavy volume expansion during long cycling processes. These drawbacks further lead to poor electrochemical/battery performances and impede their practical application [5,6]. Therefore, it is imminently to flourish suitable anode materials for SIBs and PIBs with excellent electrochemical performance.

Recently, transition metal sulfides (TMSs) and metal phosphides (TMPs) attract much attention in secondary batteries because of their delightful theoretical capacity, stable crystal structure, high electrochemical reactivity and tunability of chemical composition [7–9]. The heterogeneous structure of TMSs and TMPs with strong electronic interactions and synergistic effects will provide the abundance of active sites and the small charge transfer resistance for battery anodes. Nevertheless, there are many reports on anode materials of transition metal oxides (TMOs) and TMPs hybrids or TMOs/TMSs, but there are relatively little references on the heterostructure of TMPs and TMSs. For example, Guo *et al.* successfully synthesized Co_3O_4/CoP NFAs/CC flexible electrode material with Co_3O_4/CoP heterostructures on carbon cloth (CC) by *in-situ* phosphidation method, which demonstrated excellent electro-

* Corresponding authors.
E-mail addresses: yfzhang@gdut.edu.cn (Y. Zhang), zenglingxing@fjnu.edu.cn (L. Zeng), hsfan@gzhu.edu.cn (H. Fan).

https://doi.org/10.1016/j.cclet.2024.109796
1001-8417/

chemical properties of 769.1 mAh/g at 2.0 A/g and remarkable cycling ability of 451.3 mAh/g at 2.0 A/g around 300 cycles [10]. Sui *et al.* prepared OFC@CoS_2/CoO@rGO hybrid through the dual carbon design strategy, demonstrating excellent reversible capacity of 460 mAh/g at 0.05 A/g and remarkable cycling properties of 161 mAh/g after 3500 cycles at 1 A/g as anodes of SIBs [11]. Despite of the high theoretical specific capacity of TMSs and TMPs, they are also faced with major drawbacks such as severe volume changes and structural collapse during cycling processes, hindering their practical application as anode materials for SIBs/PIBs. Therefore, it is crucial to flourish alternative anode materials with stable structure and cycle performance. In contrast to TMSs and TMPs, metal phosphosulfide composites have been proposed as relatively advanced anode active materials, benefiting from their high Na^+ storage capacity, synergistic effect of both TMSs and TMPs, as well as the high electrochemical conductivity of sodium phosphide/sulfide originating from the charge/discharge processes [12–15]. For example, Zhao *et al.* successfully fabricated the branch-leaf-strucutured CoPS@C@N–CNF structure with stability of undergoing more than 10,000 long loops at 20.0 A/g as anodes of SIBs [16]. Dong *et al*. successfully prepared Sb|P-S@C phosphosulfide foam anode, which demonstrated a significant capacity retention capability with a specific capacity of 490 mAh/g after recirculation for 1000 cycles as anodes of SIBs [17]. Therefore, in view of the previously reported metal phosphosulfide composites with excellent electrochemical properties, the rational design of the chemical composition and structure of metal phosphosulfide anode for achieving high-property SIBs/PIBs is most important and deserves further exploration.

Metal-organic frameworks (MOFs), owing to their unique structural characteristics, excellent porosity, stable functional sites and size selectivity to guest molecules, have been demonstrated obvious advantages in various application fields such gas storage, separation, catalysis and energy storage. Recently, MOFs were proved as the hopeful precursors and templates for the design electrode materials for secondary batteries on account of their huge specific surface area and abundant pore and topological structures [18–21]. The organic ligands in MOFs were decomposed into carbon (or doped carbon) frameworks, which could provide abundant reaction active sites and favorable electrochemical performance. Interestingly, the incorporation of multi-heteroatoms (such as N, P, S, F, B) can effectively enlarge the interlayer distance for facilitating surface-related reactions and introduces rich defects and abundant active sites for the Na^+/K^+ storage [22–24]. In addition, the obtained carbon matrix also can play a significant role in the protection of the structure of electrode material from avoiding the volume expansion during the repeated Na^+/K^+ insertion/deinsertion processes. Therefore, doping heterogeneous atoms in carbon materials to improve the battery performance is a very interesting modification method. Fan *et al.* successfully fabricated $NiCo_2Se_4$⊂SPNC/CC with the reversible capacity of 268.1 mAh/g over 500 cycle at 0.5 A/g, benefiting from the N, P and S tri-doped carbon (SPNC) coating to hinder the volume expansion of $NiCo_2Se_4$ [25]. Therefore, it is worthwhile but difficult to develop MOFs-derived metal phosphosulfide and their hybrid with multi-heteroatom doping carbon matrix.

Herein, hexapod ZIF-derived cobalt phosphosulfide nanorods wrapping into multi-heteroatom-doped carbon framework (CoP/CoS_2@NPSC) were successfully fabricated using ZIF-67 as precursor and poly(hexachlorocyclophosphazene-*co*-4,4′-sulfonyldiphenol) (PZS) as N/P/S doping carbon source through synchronous phosphidation/sulfation reaction process. The PZS derived N/P/S doping carbon frameworks are conducive to Na^+/K^+ transport, effectively improve the electrochemical conductivity and provide abundant active sites. CoP/CoS_2@NPSC delivered the pleasant cycling capacity with an acceptable reversible capacity

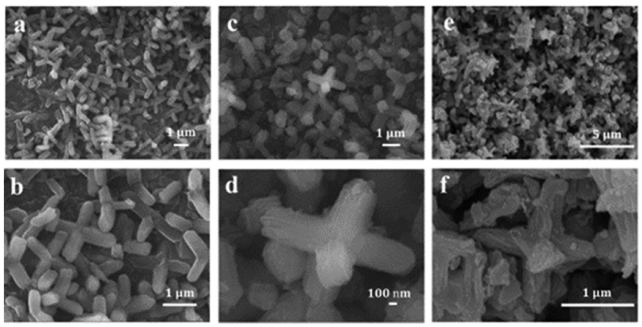

Fig. 1. SEM images of ZIF-67 (a, b), ZIF-67@PZS composite (c, d), CoP/CoS_2@NPSC (e, f).

of 597.13 mAh/g at 1.0 A/g around 100 cycles and 404.63 mAh/g at 5.0 A/g around 700 cycles with the CE of almost 100% for SIBs. Furthermore, it also displayed the specific capacity of 266.02 mAh/g at 1.0 A/g around 100 cycles and 115.33 mAh/g at 5.0 A/g around 800 cycles as an anode for PIBs.

The synthesis schematic of CoP and CoS_2 nanodots encapsulating into N/P/S tri-doped hexapod carbon framework (CoP/CoS_2@NPSC) was illustrated in Fig. S1 (Supporting information). Firstly, extremely smooth hexapod ZIF-67 precursor was successfully synthesized by using the metal Co^{2+} as the metal center, 2-methylimidazole (2MI) as the organic ligand, as well as hexadecyltrimethylammonium bromide (CTAB) as the surfactant. The obtained ZIF-67 presents uniformly hexapod structure, comprising of six cruciform nanorods vertically crossing each other with the length of about 900 nm and diameter of about 300 nm (Figs. 1a and b). Secondly, the surface of ZIF-67 was coated with a polymer layer of PZS by *in-situ* polycondensation of hexachlorocyclophosphazole (HCCP) and 4,4′-sulfobisphenol (BPS) to contrive a core-shell ZIF-67@PZS structure. SEM images in Figs. 1c and d displayed similar hexapod structure with the rough surface due to the growth of PZS layer. Finally, porous CoP/CoS_2@NPSC (Figs. 1e and f) was successfully synthesized by annealing and synchronous phosphidation/sulfation reaction, indicating the production of the small nanodots of CoP/CoS_2. In particular, the sample was contrived *via* a simple approach with a uniform and novel structure. The heteroatomic N/P/S doping carbon frameworks will greatly expand the interlayer distance and provide enough active sites, which are conductive to Na^+/K^+ adsorption, intercalation and diffusion (Fig. S1), significantly improving their electrochemical properties and battery performance by collaboration with CoP and CoS_2 nanodots.

As exhibited in the transmission electron microscopy (TEM) images (Figs. 2a-c), small CoP/CoS_2 nanodots with a size of 10 nm were uniformly encapsulated in the heteroatomic N/P/S doping hexapod carbon frameworks of CoP/CoS_2@NPSC, consisting of six "pod" with the diameter of about 300 nm. Specifically, it was known from Fig. 2d that the thickness of the external carbon layer was around 30 nm. The high-resolution transmission electron microscope (HRTEM) image (Fig. S2 in Supporting information) displayed that the amorphous carbon by PZS coating had an increased interlayer distance (∼0.39 nm) compared to those of graphite (∼0.34 nm), benefiting from the presence of abundant heteroatoms and defects, which favors the reversible insertion/extraction of Na^+ and K^+. As shown in Figs. 2e and f, it was logical to perform high-resolution tests to explore the microstructure of CoP/CoS_2@NPSC hybridization with stripe spacings of 0.17 and 0.19 nm, indexed to the (311) plane for CoS_2 and the (211) plane for CoP, respectively, which was able to correspond to the X-ray diffraction (XRD) test results. The corresponding EDS mappings (Fig. 2g) demonstrated the corresponding elements C, Co, N, P, and S are uniformly distributed into CoP/CoS_2@NPSC hybrid, fur-

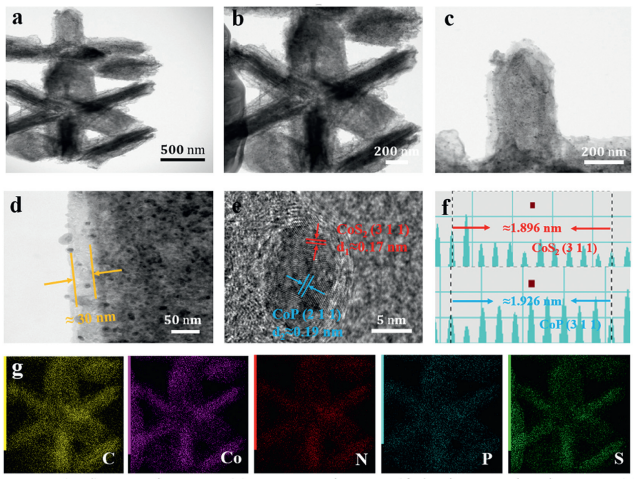

Fig. 2. (a-d) TME images, (e) HRTEM image, (f) lattice spacing images, (g) correlative element mappings of CoP/CoS_2@NPSC.

ther indicating that CoP and CoS_2 nanodots were scattered all over the hexapod framework.

The presence of CoP and CoS_2 phases in CoP/CoS_2@NPSC composites was further verified by XRD tests. Fig. S3 (Supporting information) revealed the results of the crystal structure CoP/CoS_2@NPSC, CoP/CoS_2/NC, CoP/NC, and CoS_2/NC. The diffraction peak of CoP/NC was in good agreement with CoP (JCPDS No. 29–0497), while that of CoS_2/NC corresponded to the standard card of CoS_2 (JCPDS No. 41–1471). Rightfully, two characteristic diffraction peaks of CoP/CoS_2@NPSC and CoP/CoS_2/NC were consistent with the (011), (111), (112), (211), (202) and (301) planes of CoP/NC, and the (111), (200), (210), (211), (220) and (311) planes of CoS_2/NC, indicating that CoP/CoS_2@NPSC had been successfully synthesized [26–29]. The X-ray photoelectron spectroscopy (XPS) tests were implemented in order to explore the elements and the bonding relation of as-prepared CoP/CoS_2@NPSC. The full-scan XPS spectra in Fig. 3a revealed the presence of Co, S, P, N, and C elements, showing the sample was consisted of CoS_2 and CoP. The binding energies of 284.80, 285.95 and 288.92 eV, can be assigned to C–C, C–N, and O=C, respectively, can be overtly observed in the C 1s spectra of Fig. 3b. The Co 2p spectra in Fig. 3c displayed that the peaks situated at 779.26 and 798.18 eV related to Co^{3+} and the peaks at 782.70 and 801.83 eV attributed to Co^{2+}, while two peaks situated at binding energies of 786.19 and 804.47 eV were identified as satellite peaks [30–32]. The P 2p spectra in Fig. 3d exhibited that the peak located in 129.62 eV assigned to the Co-P attributed to CoP phase, whereas the peak at 133.89 eV was denoted into P-O, corresponded to the oxidized P species because of the superfluous exposure of P to air [33–35]. The S 2p spectra in Fig. 3e exhibited that two peaks located in 163.12 eV and 163.53 eV, corresponding to S $2p_{3/2}$ and S $2p_{1/2}$ orbitals respectively. And the peak at 169.06 eV was in accord with S-O bond, which was probably attributed to the contact of CoS_2 with air [36–38]. Furthermore, it was clearly observed in the N 1s spectra (Fig. 3f), which was deconvoluted into three peaks at 398.46, 400.10 and 401.17 eV, assigned to pyridinic nitrogen, the pyrrolic nitrogen, and graphitic nitrogen, respectively [39]. In conclusion, it can be seen that the appearance of CoP/CoS_2@NPSC was successfully determined through XRD and XPS characterization results.

The mechanism of Na storage redox reaction of CoP/NC, CoS_2/NC, CoP/CoS_2/NC, and CoP/CoS_2@NPSC were performed by the incipient three-cycle cyclic voltammetry (CV) curves within 0.01–3.0 V at 0.1 mV/s. The CV curves of CoP/CoS_2/NC, CoS_2/NC, and CoP/NC were manifest in Figs. S4a, c and e (Supporting information) consistent with the first three galvanostatic charge/discharge (GCD) curves of their (Figs. S4b, d and f in Supporting information), while that of CoP/CoS_2@NPSC were demonstrated in Fig. 4a. CoP/CoS_2/NC, CoS_2/NC, and CoP/NC revealed corresponding electrochemical reaction to CoP/CoS_2@NPSC. During the initial cathodic process, the peaks close to 1.04 and 0.64 V were attributed to the generation of the solid electrolyte interphase (SEI) film and Na^+ insertion into CoP and CoS_2. In the second and third cycles, the peaks transfer to 0.92 V and 0.56 V, which was broken up into Co and P united in Na^+ to form Na_3P, and Na^+ is initially inserted into CoS_2 to cultivate Na_xCoS_2, and therewith Na^+ reacts with Na_xCoS_2 to cultivate Co and Na_2S. The oxidation peaks closed to 1.73 and 1.96 V related to the de-sodium reactions of Na_3P and Na_2S during the anodic scan [40–42]. The pattern of the curves was virtually overlapped different with the initial cycle due to the existence of SEI film, suggesting that CoP/CoS_2@NPSC electrode displayed great cycling stability. Combined with the first three GDC profiles of CoP/CoS_2@NPSC within the voltage window from 0.01 V to 3.0 V at 0.1 A/g, it can be observed that the platform from 2.00 V to 0.50 V consistent with CV curves was shown in Fig. 4b. Furthermore, the first capacity of CoP/CoS_2@NPSC is 790.22/670.91 mAh/g with a great initial Coulombic efficiency (ICE) of 84.90%, and the profiles the subsequent cycles almost overlap, indicating that it is an outstanding electrode material. Fig. 4c displayed GCD curves of CoP/CoS_2@NPSC at current densities between 0.1 A/g to 5.0 A/g, which proffers congruous plateau locations regardless of the diverse current densities, suggesting acceptable conductivity. As illustrated in Fig. 4d, the rate capability of CoP/NC, CoS_2/NC, CoP/CoS_2/NC, and CoP/CoS_2@NPSC as anodes for SIBs were performed at rising current densities between 0.1 A/g and 5.0 A/g for every five cycles, where CoP/CoS_2@NPSC displays better rate capability as opposed to CoP/NC, CoS_2/NC, and CoP/CoS_2/NC. CoP/CoS_2@NPSC displayed reversible discharge capacities of 623.94, 607.03, 569.68, 537.10, 509.59, and 474.15 mAh/g at 0.1, 0.2, 0.5, 1.0, 2.0, and 5.0 A/g, respectively. The rate capability can return to 612.50 mAh/g, while the current density reverts to 0.1 A/g. More importantly, CoP/CoS_2@NPSC showed a great advantage in rate performance compared to previously reported CoS_2 or CoP anode materials (Fig. 4e) [43–47]. CoP/NC, CoS_2/NC, and CoP/CoS_2/NC had impecunious cycling capacity with merely 181.45, 395.83, and 406.68 mAh/g at 1.0 A/g after 100 cycles, while CoP/CoS_2@NPSC had pleasant cycling capacity with 597.13 mAh/g at the same conditions (Fig. 4f). Furthermore, CoP/CoS_2/NC had capacity of 330.56 mAh/g at 5.0 A/g around 700 cycles with ICE of 75.04% (625.47/469.33 mAh/g), while CoP/CoS_2@NPSC kept a pleasant capacity of 404.63 mAh/g at the same conditions with higher ICE of 87.35% (692.69/605.09 mAh/g) and CE of almost 100% (Fig. 4g). Therefore, compared to CoP/NC, CoS_2/NC, and CoP/CoS_2/NC, CoP/CoS_2@NPSC has potential rate capability and stable long cycle performance. The significant enhancement of the electrochemical performance of CoP/CoS_2@NPSC electrodes is attributed to the synergistic effect of doped N/P/S atoms and collaboration with CoP and CoS_2 nanodots.

The reaction mechanism of CoP/CoS_2@NPSC was investigated using *ex-situ* XRD method and displayed in Fig. 5a. Obviously, the diffraction peaks of CoP and CoS_2 were significantly reduced and Na_3P and Na_2S emerged when the battery was discharged to 1.0 V. With the continued discharge to 0.01 V, the CoP and CoS_2 phases disappeared, while the peak of metal Co was clearly present. During the charging process, the peak of metal Co were not observed while the peak of CoP and CoS_2 reappear again especially at 3.0 V, but the peak of Na_3P and Na_2S still existed at the voltage, implying that the transformation reactions occurring in the CoP and CoS_2 phases were not completely reversible [47–49]. To scrutinize the electrochemical energy storage mechanism of CoP/CoS_2@NPSC in SIBs, the *ex-situ* XPS technique was adopted for in-depth analysis.

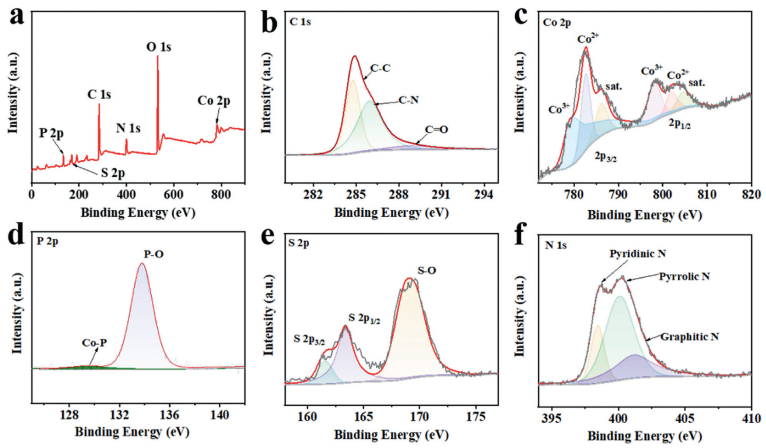

Fig. 3. (a) XPS survey spectrum of CoP/CoS_2@NPSC. XPS spectra of (b) C 1s in CoP/CoS_2@NPSC. (c) XPS spectra of (b) Co 2p in CoP/CoS_2@NPSC and CoP/CoS_2/NPSC. (d-f) XPS spectra of P 2p, S 2p, and N 1s in CoP/CoS_2@NPSC.

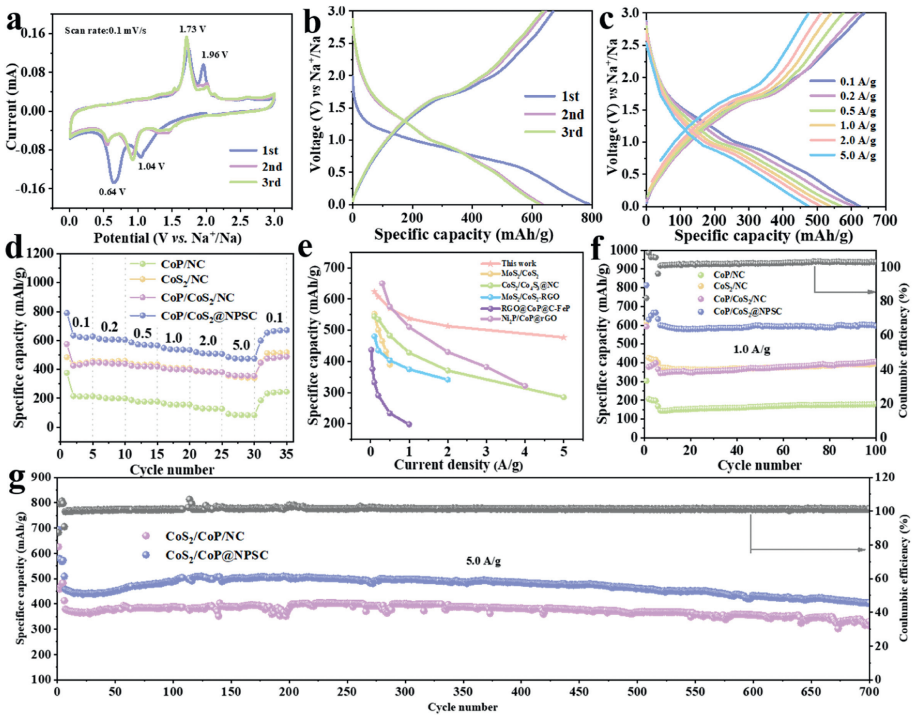

Fig. 4. The sodium storage performance of CoP/CoS_2@NPSC: (a) CV profiles for the 1^{st}-3^{rd} cycles under 0.1 mV/s. (b) GCD curves for the 1^{st}-3^{rd} cycles at 0.1 A/g. (c) GCD curves. (d) Rate capacity of CoP/CoS_2@NPSC, CoP/CoS_2/NC, CoS_2/NC and CoP/NC. (e) Compared to rate performance of similar materials. (f) Cycle performance of CoP/CoS_2@NPSC, CoP/CoS_2/NC, CoS_2/NC and CoP/NC at 1.0 A/g. (g) Cycle performance of CoP/CoS_2@NPSC and CoP/CoS_2/NC at 5.0 A/g.

Fig. 5b showed the Co 2p spectra in different states. After discharging to 1.2 V, the binding energy spectrum of Co 2p can be split into four crucial peaks situated at 780.27, 784.01, 796.05, and 801.32 eV, consistent with Co^{3+} $2p_{3/2}$, Co^{2+} $2p_{3/2}$, Co^{3+} $2p_{1/2}$, and Co^{2+} $2p_{1/2}$ and two satellite peaks were situated at 787.69 and 803.66 eV, respectively. The existence of Co^{3+} can be consistent with the fact that the metallic Co^0 is easily oxidized to Co_3O_4 on the surface layer in the occurrence of the transformation reaction, which makes the Co^0 peak hard to expose. Moreover, Co^{2+} $d_{1/2}$ tapers off during the process of discharge, because Co ion undergoes reduction [50,51]. For S 2p spectra (Fig. S5 in Supporting information), the peaks at approximately 161.58/162.53 eV were attributed to S^{2-}, when that at approximately 163.16/164.49 eV were attributed to S_n^{2-}. In addition, located at approximately 168.19/169.48 eV were assigned to the presence of sulfate [52]. The imparity in the position of the peak about S 2p spectra are attributed to the fact that element S takes place a redox reaction. The XPS spectra of P 2p was revealed in Fig. S6 (Supporting information). It is clearly observed that Co-P bond disappeared quite obviously at approximately 128.43 eV and could not return to the pristine state at 2.5 V charging state when the battery was discharged from 1.2 V to 0.01 V, which suggests an irreversible redox reaction and consistent with the CV curve [53]. Fig. 5c presented *ex-situ* electrochemical impedance spectroscopy (EIS) curves of CoP/CoS_2@NPSC under different selection potentials in the first (de)sodiation process. When it was discharged from OCV to 1.0 V, the R_{ct} increased, caused by volume expansion when Na^+ was inserted. When it was continuously discharged to 0.5 V, the R_{ct} continued to increase due to the generation of SEI film, which was corresponded to the analysis judgement of CV. During the charging process, the R_{ct} became smaller and smaller than that of the initial sample with the increase of voltage, indicating that the initial electrochemical proce-

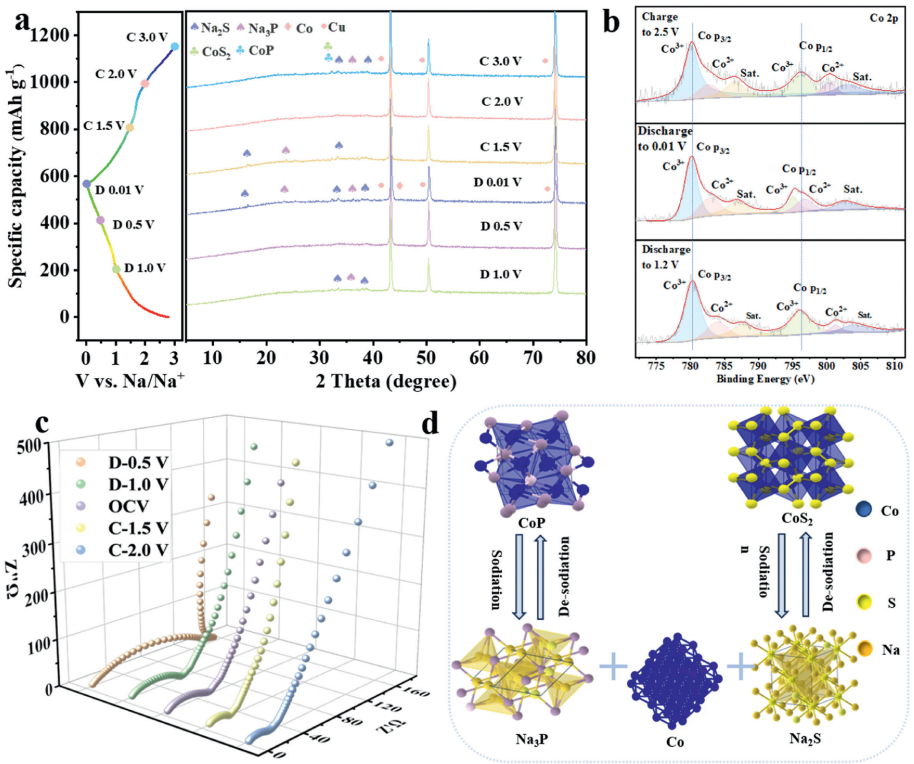

Fig. 5. *Ex-situ* characterization of (a) XRD patterns. (b) XPS spectra of Co 2p. (c) EIS test at different status in the primary cycle. (d) Energy storage mechanisms in the primary cycle.

dure of CoP/CoS_2@NPSC is not completely reversible [54]. The possible transformation mechanism of CoP/CoS_2@NPSC was shown in Fig. 5d, more concretely and explicitly illustrating the phase change in the (de)sodiation process.

The *pseudo*-capacitive nature of CoP/CoS_2@NPSC electrode was performed by CV loop at diverse scan rates of 0.1–1.0 mV/s, as revealed in Fig. S7a (Supporting information), where the obvious peaks with similar shapes have a slight shift, suggesting that CoP/CoS_2@NPSC has the remarkable reversibility and slight polarization. The linear correlation between the peak current (i) and the scanning rate (v) can be expressed by the formula, that is $i = av^b$, where b can reflect the electrochemical mechanism of CoP/CoS_2@NPSC electrode. Specifically, b approaches 0.5, indicating that the electrochemical process stands for diffusion behavior, when b approaches 1.0, indicating that *pseudo*-capacitor behavior is dominant [56]. The corresponding b values of each peak were 0.85, 0.96, 0.75, and 1.04 in Fig. S7b (Supporting information), respectively, which indicates the electrochemical process of CoP/CoS_2@NPSC electrode is obviously commanded by *pseudo*-capacitor behavior. From the formula: $i(V) = K_1 + K_2v^{1/2}$ [55], we can calculate *pseudo*-capacitive contributions of that in Fig. S7c (Supporting information), which were 88.31%, 89.41%, 91.77%, 93.71%, 94.46%, and 96.13% consistent with the sweep ratio of 0.1, 0.2, 0.4, 0.6, 0.8, and 1.0 mV/s, respectively, suggesting the increased pseudocapacitive behavior with the improving scanning rate. Concretely, the *pseudo*-capacitive contribution of CoP/CoS_2@NPSC electrode was 91.77%, while diffusion only possesses 8.23% at 0.4 mV/s (Fig. S7d in Supporting information). The galvanostatic intermittent titration technique (GITT) is a significant method to measure the Na^+ diffusion coefficient of CoP/CoS_2@NPSC (Fig. S7e in Supporting information), where exhibits a complete GCD process of the second cycle in the GITT experimental test in the voltage range of 0.01–3.0 V and the current maintained at 0.1 A/g. Fig. S7f (Supporting information) revealed an enlarged plot of the amplified potential response of CoP/CoS_2@NPSC electrode during a single current pulse. According to this criterion: $D_{Na^+} = \frac{4}{\pi\tau}(\frac{mV_M}{MA})^2(\frac{\Delta E_s}{\Delta E_\tau})^2$, the diffusion coefficient of Na^+ can be calculated. The reduction of D_{Na^+} signifies the improved intercalation process of Na^+, ascribed to the chemical conversion reaction [56,57]. As depicted in Figs. S7g and h (Supporting information), it can be obviously seen that there was a considerable transform in the D_{Na^+} with nearly 0.90 V in the discharging course and 1.70 V in the charging course, corresponding to the consequences of CV loop. In order to better understand the excellent Na storage properties of CoP/CoS_2@NPSC, EIS tests were conducted to further understand its reaction kinetics. As shown in Fig. S7i (Supporting information), the consequences of EIS are adduced as Nyquist plots with related equivalent circuits. The reaction kinetics of the CoP/CoS_2@NPSC electrode was investigated further by exploring the value of EIS. The R_{ct} was less than that of the uncirculated cycle after 50 cycles, implying that the charge shift kinetics of the CoP/CoS_2@NPSC electrode was increased during the cycling process.

CoP/CoS_2@NPSC electrode was further used as an anode in PIB because of electrochemical properties of that in SIBs. Fig. 6a exhibited the initial three CV loops of CoP/CoS_2@NPSC to examine the chemical reactions that take place regarding potassium storage. An expansive peak appeared at 0.62 V, ascribing to the presence of SEI film about the discharge of the first lap, which was also associated with K^+ insertion into CoP and CoS_2, cultivating K_3P and K_2S. The oxidation peaks closed to 1.26 and 1.87 V related to the de-potassium reactions of K_3P and K_2S during the anodic scan. Combined with the first three GDC profiles of CoP/CoS_2@NPSC between 0.01 V and 3.0 V at 0.1 A/g, it can be observed that the platform from 1.90 V to 0.60 V consistent with CV curves was shown in Fig. 6b. Furthermore, the first capacity of CoP/CoS_2@NPSC was 1699.28/704.51 mAh/g with the initial CE of 41.46% when that of CoP/CoS_2/NC merely had 1637.22/459.39 mAh/g with CE of 28.06%

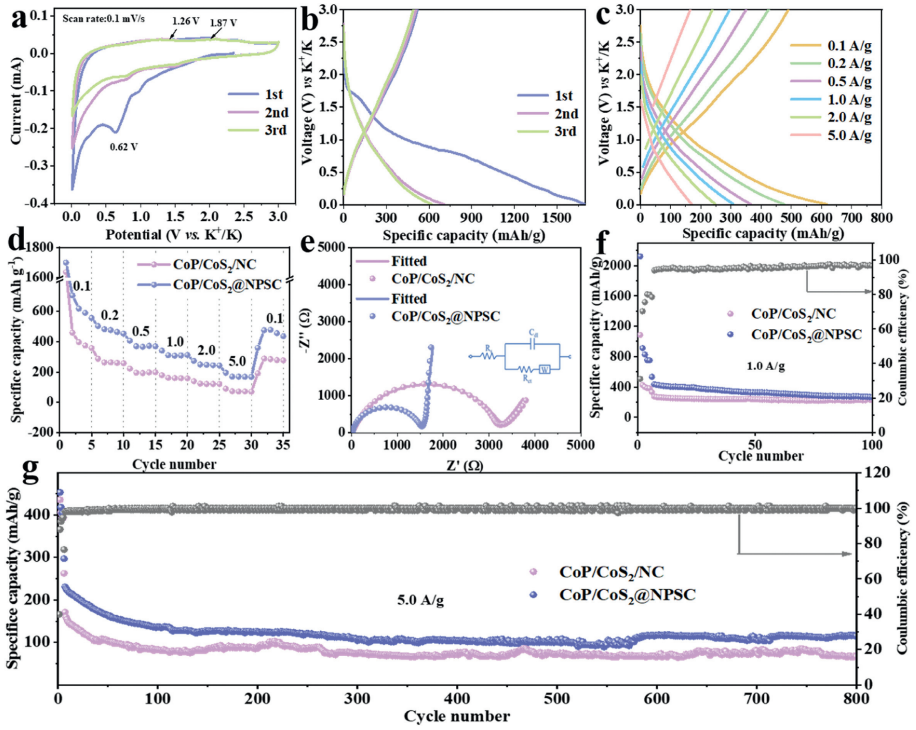

Fig. 6. The potassium storage performance of CoP/CoS_2@NPSC: (a) CV profiles and (b) GCD curves for the 1st-3rd cycles under 0.1 mV/s. (c) GCD curves at different current densities. (d) Rate capacity, (e) Nyquist curves, cycle performance (d) at 1.0 A/g and (g) at 5.0 A/g of CoP/CoS_2@NPSC and CoP/CoS_2/NC.

(Fig. S8 in Supporting information), and the profiles the subsequent cycles almost overlap, indicating that it is a potential anode material for PIBs. Fig. 6c displayed GCD curves of CoP/CoS_2@NPSC at current densities between 0.1 A/g to 5.0 A/g, which proffers congruous plateau locations regardless of the diverse current densities, suggesting acceptable conductivity. As illustrated in Fig. 6d, CoP/CoS_2@NPSC displayed reversible discharge capacities of 617.78, 476.25, 366.18, 307.94, 247.83, and 169.31 mAh/g at 0.1, 0.2, 0.5, 1.0, 2.0, and 5.0 A/g, respectively. The rate capability can return to 478.13 mAh/g, while the current density reverted to 0.1 A/g. The reaction kinetics of the CoP/CoS_2@NPSC was investigated by exploring the value of EIS, whose R_{ct} (29.33 Ω) was less than that of CoP/CoS_2/NC (40.75 Ω) (Fig. 6e). Therefore, it can be obviously observed from the EIS results that CoP/CoS_2@NPSC presents the higher conductivity in comparison with CoP/CoS_2/NC. CoP/CoS_2/NC had impecunious cycling capacity merely 226.91 mAh/g at 1.0 A/g around 100 cycles, while CoP/CoS_2@NPSC had pleasant cycling capacity of 266.02 mAh/g at the same conditions (Fig. 6f). Furthermore, CoP/CoS_2/NC had capacity of 66.69 mAh/g at 5.0 A/g around 800 cycles, while CoP/CoS_2@NPSC held the pleasant capacity of 115.33 mAh/g at the same conditions with the CE of almost 100% (Fig. 6g).

In conclusion, hexapod cobalt phosphosulfide nanorods encapsulating into N/P/S tri-doped hexapod framework (CoP/CoS_2@NPSC) were successfully fabricated using ZIF-67 as precursor and PZS as N/P/S doping carbon source through synchronous phosphidation/sulfation reaction process. The synergistic effect between CoP and CoS_2, as well as the CoP/CoS_2 and the NPSC carbon framework can increase the conductivity. The NPSC carbon framework not only serves to protect the hexapod framework, but also avoids the aggregation of internal CoP and CoS_2 nanodots. Besides, the kinetics analysis demonstrated that the nitrogen, phosphorus, sulfur tri-doping could greatly increase the interlayer distance and introduce enough active sites, which effectively facilitate the transport, adsorption, insertion and diffusion of Na^+ and K^+. CoP/CoS_2@NPSC delivered excellent cycle stability of 404.63 mAh/g at 5.0 A/g around 700 cycles for SIBs and 115.33 mA/g at 5.0 A/g around 800 cycles for PIBs. This approach provides some advanced insights into the preparation of ZIF-derived metal phosphosulfide for SIBs and PIBs anode materials with improved electrochemical performance.

Declaration of competing interest

The authors declare that they have no known competing financial interests or personal relationships that could have appeared to influence the work reported in this paper.

Acknowledgments

This work was supported by the National Natural Science Foundation of China (Nos. 52472194, 52101243), Natural Science Foundation of Guangdong Province, China (No. 2023A1515012619) and the Science and Technology Planning Project of Guangzhou (No. 202201010565). We would like to thank Analysis and Test Center of Guangzhou University for their technical support (XRD, ANTO PAAR, TTK600).

Supplementary materials

Supplementary material associated with this article can be found, in the online version, at doi:10.1016/j.cclet.2024.109796.

References

[1] P.F. Wan, X.L. Peng, S.Y. Dong, et al., J. Colloid Interface Sci. 657 (2024) 757–766.
[2] P. Xia, S. Li, L. Yuan, et al., J. Membr. Sci. 694 (2024) 122395.
[3] X. Cui, J.X. Chen, Z.F. Sun, et al., Adv. Funct. Mater. 33 (2023) 2212100.
[4] J. Xiong, X.Y. Liu, P. Xia, et al., J. Colloid Interface Sci. 652 (2023) 1417–1426.
[5] L. Zhang, W. Wang, X. Ma, S. Lu, Y. Xiang, Nano Today 37 (2021) 101074.
[6] T.Y. Wang, S.Q. Chen, H. Pang, H.G. Xue, Y. Yu, Adv. Sci. 4 (2017) 1600289.
[7] R. Sun, F. Xu, C.H. Wang, et al., Rare Met. 43 (2024) 1906–1931.

[8] D. Chen, Y. Wu, Z. Huang, et al., Chem. Eng. J. 457 (2023) 141181.
[9] X. Cui, M.X. Liang, L. Wang, et al., Batter. Supercaps 6 (2022) e202200271.
[10] C. Zhao, L. Zhang, S. Jing, et al., ACS Appl. Mater. Interfaces 15 (2023) 23217–23225.
[11] R. Sui, G. Zan, M. Wen, et al., ACS Appl. Mater. Interfaces 14 (2022) 28004–28013.
[12] X. Xu, S. Wang, S. Guo, et al., Adv. Powder Mater. 1 (2022) 100027.
[13] X. Chen, X. Ding, H. Muheiyati, et al., Nano Res. 12 (2019) 1115–1120.
[14] S. Su, L. Sun, J. Qian, X. Shi, Y. Zhang, ACS Appl. Energy Mater. 5 (2021) 685–696.
[15] K. Maiti, K. Kim, K.J. Noh, J.W. Han, Chem. Eng. J. 423 (2021) 130233.
[16] W. Zhao, X. Ma, L. Gao, et al., Adv. Mater. (2023) 1–14.
[17] S. Dong, C. Li, Z. Li, et al., Energy Stor. Mater. 20 (2019) 446–454.
[18] F. Xu, S.L. Li, S.D. Jing, et al., J. Colloid Interface Sci. 660 (2024) 907–915.
[19] S.M. Wu, W. Yang, Z.T. Liu, et al., J. Colloid Interface Sci. 660 (2024) 97–105.
[20] C. Ke, R. Shao, Y. Zhang, et al., Adv. Funct. Mater. 32 (2022) 2205635.
[21] P. Wan, S. Dong, J. Xiong, et al., J. Colloid Interface Sci. 650 (2023) 582–592.
[22] P. Li, H.C. Zeng, Chem. Commun. 53 (2017) 6025–6028.
[23] X. Liu, Y. Tong, Y. Wu, et al., Chem. Eng. J. 431 (2022) 133986.
[24] S. Wu, F. Xu, Y. Li, et al., J. Colloid Interface Sci. 649 (2023) 741–749.
[25] J. Fan, Y. Zheng, Z. Zhao, W. Guo, S. Zhu, Front. Mater. 9 (2022) 875684.
[26] K. Xie, L. Li, X. Deng, W. Zhou, Z. Shao, J. Alloy. Compd. 726 (2017) 394–402.
[27] Q. Li, S. Dong, Y. Zhang, et al., Eur. J. Inorg. Chem. 2018 (2018) 3433–3438.
[28] S. Luo, C. Zheng, W. Sun, et al., Electrochim. Acta 289 (2018) 94–103.
[29] Q. Chang, Y. Jin, M. Jia, et al., J. Colloid Interface Sci. 575 (2020) 61–68.
[30] Z. He, H. Xu, L. Shi, et al., Small (2023) 1–10.
[31] Y. Pan, Y. Fang, H. Jin, et al., Electrocatalysis 10 (2019) 253–261.
[32] B. Cheng, B. Wang, H. Lei, et al., J. Colloid Interface Sci. 643 (2023) 574–584.
[33] X. Hu, S. Zhang, J. Sun, et al., Nano Energy 56 (2019) 109–117.
[34] S. Tao, J. Xu, T. Xie, et al., J. Power Sources 500 (2021) 229975.
[35] H. Sun, J. Wang, W. Li, et al., Electrochim. Acta 388 (2021) 138628.
[36] W. Zhang, Z. Yue, Q. Wang, et al., Chem. Eng. J. 380 (2020) 122548.
[37] F. Xiao, X. Yang, D. Wang, et al., ACS Appl. Mater. Interfaces 12 (2020) 12809–12820.
[38] P. Huang, H. Ying, S. Zhang, Z. Zhang, W.Q. Han, Chem. Eng. J. 429 (2022) 132396.
[39] X. Zhao, D. Luo, Y. Wang, Z.H. Liu, Nano Res. 12 (2019) 2872–2880.
[40] T. Wu, S. Zhang, Q. He, et al., ACS Appl. Mater. Interfaces 9 (2017) 28549–28557.
[41] X. Wang, X. Li, Q. Li, et al., Nano-Micro Lett. 10 (2018) 46.
[42] B. Qin, M. Wang, S. Wu, et al., Chin. Chem. Lett. 35 (2024) 108921.
[43] C. Dong, L. Guo, H. Li, et al., Energy Stor. Mater. 25 (2020) 679–686.
[44] Z. Li, L. Zhang, X. Ge, et al., Nano Energy 32 (2017) 494–502.
[45] J. Liu, Y.G. Xu, L.B. Kong, J. Colloid Interface Sci. 575 (2020) 42–53.
[46] Y. Su, C. Wu, H. Li, et al., J. Alloy. Compd. 845 (2020) 156229.
[47] H. Zhou, Y. Zhao, Y. Jin, et al., J. Power Sources 560 (2023) 232715.
[48] R. Zhuang, Z. Huang, S. Wang, et al., Chem. Eng. J. 409 (2021) 128235.
[49] Z. Jiang, S. Li, Y. Chen, et al., Nanoscale 15 (2023) 12296–12306.
[50] X.T. Li, H.J. Liang, B.Y. Qin, et al., J. Colloid Interface Sci. 625 (2022) 41–49.
[51] M. Tao, G. Du, T. Yang, et al., J. Mater. Chem. A 8 (2020) 3018–3026.
[52] Q. Wu, Y. Zhang, Y. Lin, et al., ACS Appl. Mater. Interfaces 15 (2023) 46971–46981.
[53] G. Xu, X. Kang, H. Yin, et al., ACS Appl. Mater. Interfaces (2023) 52485–52495.
[54] S. Chen, F. Wu, L. Shen, et al., ACS Nano 12 (2018) 7018–7027.
[55] S.J. Lu, J.Y. Lin, C.H. Wang, et al., Rare Met. 43 (2024) 3713–3723.
[56] L. Xing, K. Han, Q. Liu, et al., Energy Storage Mater 36 (2021) 309–317.
[57] S. Iqbal, L. Wang, Z. Kong, et al., ACS Appl. Mater. Interfaces 666 (2024) 416–423.